arXiv:1701.05528v1 [cond-mat.str-el] 19 Jan 2017

Rearrangement of Van-der-Waals Stacking and Formation of a Singlet State at $T = 90\,\mathrm{K}$ in a Cluster Magnet

John P. Sheckelton,[a,b] Kemp W. Plumb,[b] Benjamin A. Trump,[a,b] Collin L. Broholm,[b,c,d] and Tyrel M. McQueen[a,b,c,*]

Insulating Nb_3Cl_8 is a layered chloride consisting of two-dimensional triangular layers of $S_{eff} = 1/2$ Nb_3Cl_{13} clusters at room temperature. Magnetic susceptibility measurement show a sharp, hysteretic drop to a temperature independent value below $T = 90\,\mathrm{K}$. Specific heat measurements show that the transition is first order, with $\Delta S \approx 5\ \mathrm{J \cdot K^{-1} \cdot mol}\, f.u.^{-1}$, and a low temperature T-linear contribution originating from defect spins. Neutron and X-ray diffraction show a lowering of symmetry from trigonal $P\bar{3}m1$ to monoclinic $C2/m$ symmetry, with a change in layer stacking from -AB-AB- to -AB′-BC′-CA′- and no observed magnetic order. This lowering of symmetry and rearrangement of successive layers evades geometric magnetic frustration to form a singlet ground state. It is the lowest temperature at which a change in stacking sequence is known to occur in a Van-der-Waals solid, occurs in the absence of orbital degeneracies, and suggests that designer 2-D heterostructures may be able to undergo similar phase transitions.

1 Introduction

Emergent phenomena among strongly interacting atoms or electrons, such as superconductivity[1–3], charge density waves[4], topological insulators[5,6], Kondo insulators[7,8], and heavy fermions[9], are at the forefront of contemporary materials research. Geometrically frustrated magnets are a particularly illustrative class of strongly interacting systems where a large degeneracy of electronic states exist within a small energy regime compared to the magnetic interaction strength. Since the electronic degeneracy arises from lattice symmetry, geometrical frustration can destabilize the lattice. Here we show that a geometrically frustrated antiferromagnet built from small transition metal clusters[10–15] can succumb to a symmetry-lowering distortion to evade a degenerate magnetic ground state, even in the absence of orbital degeneracies. This phase change also involves a change in stacking sequence between successive charge-neutral Van-der-Waals (VdW) bonded layers.

Specifically, we report the discovery of a paramagnetic and trigonal to singlet and monoclinic phase

[a] *Department of Chemistry, The Johns Hopkins University, Baltimore, MD 21218, USA.*
[b] *Institute for Quantum Matter and Department of Physics and Astronomy, The Johns Hopkins University, Baltimore, MD 21218, USA.*
[c] *Department of Materials Science and Engineering, The Johns Hopkins University, Baltimore, Maryland 21218, USA.*
[d] *NIST Center for Neutron Research, National Institute of Standards and Technology, Gaithersberg, MD 20899, USA.*
* E-mail: *mcqueen@jhu.edu*

transition in the cluster-based magnet Nb_3Cl_8, despite each Nb_3Cl_{13} cluster harboring a singly occupied, non-degenerate highest occupied molecular orbital (HOMO) and an approximately 1 eV gap to degenerate lowest unoccupied molecular orbital (LUMO) states. As for Mo_3O_{13} clusters in $LiZn_2Mo_3O_8$ [10], a formal electron count yields one $S_{eff} = 1/2$ magnetic electron per Nb_3Cl_{13} cluster, which are arranged on a two-dimensional triangular lattice. Nb_3Cl_8 and various stacking variations [16–20] have been previously studied. The α-Nb_3Cl_8 polymorph, with -AB-AB- stacking, is known to undergo a hysteretic magnetic transition [21] with a change in the magnetic signal at temperatures below $T \approx 90$ K. Here, this transition is studied *via* detailed structural and physical property investigations of both powder and single crystals, revealing a dramatic trigonal to monoclinic phase transition at $T = 90$ K that quenches the magnetic response but without magnetic order, *i.e.* a singlet state. The relief of geometric frustration *via* orbital ordering and formation of magnetic order or spin singlets, is well-known in compounds containing first-order Jahn-Teller (FOJT) active ions or clusters, such as $NaTiO_2$ [22,23], $NaVO_2$ [24], or $GaNb_4S_8$ [25]. A similar spin-Peierls distortion in 1D $S_{eff} = 1/2$ systems, such as $CuGeO_3$ [26], $NaTiSi_2O_6$ [27], and the titanium oxychlorides/oxybromides [28,29], can also be explained in terms of orbital ordering [30].

The phase transition to evade geometric magnetic frustration in Nb_3Cl_8 appears to proceed *via* a different route. The structural phase transition breaks the C_{3v} symmetry of the Nb_3Cl_{13} clusters in a manner consistent with a second-order Jahn-Teller (SOJT) distortion, but with a dramatic change in Nb_3Cl_8 layer stacking from -AB-AB- to -AB′-BC′-CA′-. That such a change in stacking of a VdW material can occur near liquid nitrogen temperature is remarkable, but can be thought of as being driven by a buckling of interfacial Cl-atom layers due to an inter-layer electronic interaction and SOJT distortion combined with singlet formation. Our results demonstrate the importance of considering multi-site effects and states far from the HOMO in magnetically frustrated materials, and that changes in VdW stacking sequence are possible well below room temperature.

2 Methods

Single crystalline Nb_3Cl_8 was synthesized by self vapor transport in an evacuated quartz tube charged with a stoichiometric amount of twice re-sublimed $NbCl_5$ (Strem, 99.99%) and powder Nb metal, used as is (Alfa, 99.99%). A temperature gradient of $T = 825^oC$ to $T = 835^oC$ was maintained over the reaction vessel for 12 to 14 days before cooling to room temperature. All samples were handled in a glovebox using standard air-free techniques. High-resolution synchrotron X-ray diffraction measurements (SXRD) were taken on powder samples of ground single crystals at temperatures from $T = 300$ K to $T \approx 90$ K using the powder diffractometer at beamline 11-BM equipped with a liquid nitrogen cryostream at the Advanced Photon Source (APS). Triple-axis Neutron diffraction measurements of co-aligned Nb_3Cl_8 single crystals were acquired from $T = 300$ K to $T = 1.6$ K on the SPINS spectrometer at the NIST Center for Neutron Research (NCNR). SPINS was operated with a fixed energy of 5 meV, flat analyzer, and a ^{58}Ni guide - 80' - 40' - open collimation sequence.

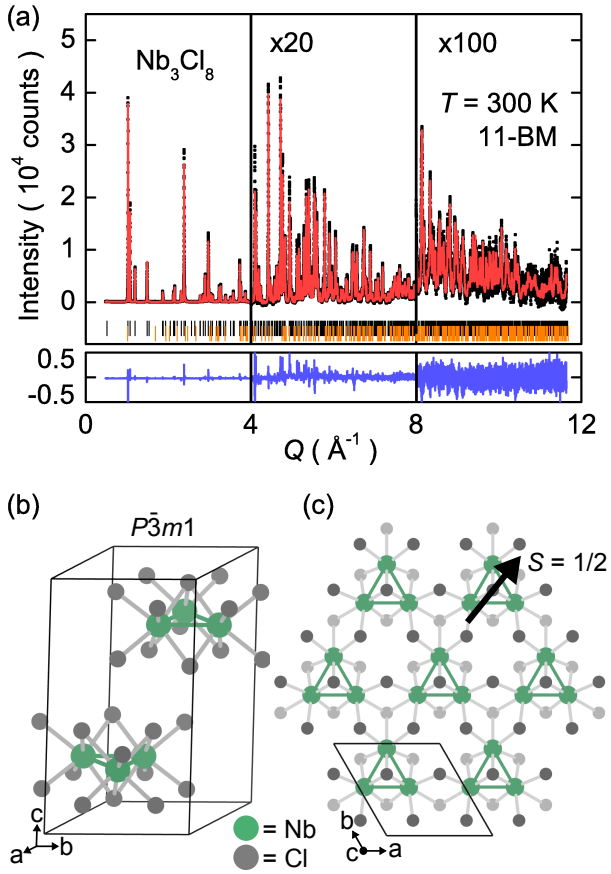

Figure 1 (a) Rietveld analysis of synchrotron X-ray diffraction data at T = 300 K. Black dots are data, red line is the calculated fit, blue line is the difference, tick marks are Bragg reflections for Nb_3Cl_8 (black) and a minor impurity, $NbOCl_2$ (orange, 0.3(2) wt%). The higher Q data are multiplied $\times 20$ ($4 \geq Q \geq 8$) and $\times 100$ ($8 \geq Q \geq 12$). The resulting unit cell of the Rietveld analysis is shown in (b) and (c). There are two Nb_3Cl_{13} clusters per unit cell with each cluster composed of three edge-sharing $NbCl_6$ octahedra meeting at an apical Cl atom atop the Nb_3 triangle. The resulting Nb_3Cl_8 layers are inequivalent as can be seen by the alternating direction of the capping Cl atom and thus form an -AB-AB- stacking sequence. A single *ab*-plane of Nb_3Cl_8 is shown in (c), forming a triangular lattice of S_{eff} = 1/2 triangular clusters.

Measurements were performed with the Nb_3Cl_8 single crystal array oriented in both the (*hhl*) or (*h*0*l*) scattering planes of the high temperature structure. Low-temperature powder X-ray diffraction (PXRD) patterns were acquired from $T = 300$ K to $T = 12$ K using a Bruker D8 Advance powder diffractometer with Cu$K\alpha$ radiation ($\lambda = 1.5424$ Å), a scintillator point detector with 0.6 mm slits, and an Oxford Cryosystems PheniX low-temperature closed cycle cryostat. Powder neutron diffraction at $T = 300$ K and $T = 10$ K was performed at the POWGEN diffractometer, Spallation Neutron Source, Oak Ridge National Laboratory (ORNL). Scans were measured for 4 hours each on a 0.2 g sample of crushed Nb_3Cl_8 single crystals. Rietveld refinements to synchrotron and in-house X-ray diffraction data were performed using the General Structure Analysis System (GSAS)[31] and the commercial Bruker Topas software suite. Refinement to the low-temperature powder neutron diffraction data was performed using the program FAULTS[32] software package to account for random HT-phase stacking faults (-AB-AB-) in the LT phase. Angle dependent magnetic susceptibility measurements

on single crystalline Nb_3Cl_8 were performed on a Quantum Design Physical Properties Measurement System (PPMS) from $T = 300\,\mathrm{K}$ to $T = 2\,\mathrm{K}$ under an applied field of $\mu_o H = 5\,\mathrm{T}$, after first measuring the sample holder temperature dependent background, which was subsequently subtracted from the data. Specific heat capacity measurements were taken on a PPMS from $T = 300\,\mathrm{K}$ to $T = 2\,\mathrm{K}$ using the semi-adiabatic pulse technique and dual slope analysis method. For sensitivity to latent heat, measurements around $T \approx 90\,\mathrm{K}$ were performed using a single large heat pulse from $T = 85\,\mathrm{K}$ to $T = 110\,\mathrm{K}$, and analyzed *via* the multi-point single slope method[33]. Resistivity measurements were taken using the four-probe method in the PPMS by attaching Pt wire to single crystalline Nb_3Cl_8 using DuPont 4922N silver composition paint. The sample was measured from $T = 300\,\mathrm{K}$ to $T \approx 275\,\mathrm{K}$ where the resistivity exceeded the instrument threshold due to a voltmeter impedance of $\approx 16\,\mathrm{M\Omega}$. Band structure calculations were performed on the high- and low-temperature phases of Nb_3Cl_8. Convergence was achieved with a $8\times8\times4$ and $4\times7\times4$ k-point mesh for the high- and low-temperature phases respectively, using the ELK all-electron full-potential linearized augmented-plane wave (FP-LAPW) code using the Perdew-Wang/Ceperley-Alder LSDA functional[34].

3 Results

Results of Rietveld refinements to powder SXRD data at $T = 300\,\mathrm{K}$ of the high-temperature (HT) $P\bar{3}m1$ phase are shown in Fig. 1. The HT phase unit cell [Fig. 1 (b)] consists of two Nb_3Cl_{13} clusters per unit cell in a -AB-AB- bilayer stacking order where A and B refer to independent Nb_3Cl_8 layers and AB constitutes a single bilayer, since adjacent Nb_3Cl_8 layers are inequivalent due to alternating directions of the Nb_3 capping Cl atoms. No atoms occupy the two inequivalent spaces between Nb_3Cl_8 layers, leaving only Van-der-Waals (VdW) interactions between interfacial Cl layers as the net attractive force. Rietveld refinement to powder synchrotron diffraction data [Fig. 1 (a)] show low-Q diffraction peaks that are asymmetric and not fit well (broad calculated peaks) due to a combination of instrumental low angle peak asymmetry and significant stacking faults. The excellent overall quality of the fit is highlighted by the zoomed regions. To assess whether or not a more subtle distortion is present at high temperatures, fits to space groups with symmetry elements systematically removed ($P\bar{3}$, $P3m$, $P3$, and $C2/m$) do not improve the fit, either statistically or qualitatively. The low temperature synchrotron data near $T \approx 90\,\mathrm{K}$ show no indication of a symmetry-lowering structural distortion (see ESI†). These results from the HT phase are in agreement with the structure previously inferred from single crystal X-ray diffraction[19,35].

The temperature dependent magnetic susceptibility of single crystalline Nb_3Cl_8 upon cooling and warming is shown in Fig. 2 (a) for fields parallel and perpendicular to the c crystallographic axis. Whereas previous reports show that Nb_3Cl_8 has hysteretic magnetization with a clear transition around $T \approx 90\,\mathrm{K}$[21], we find the susceptibility effectively vanishes for $T < 90\,\mathrm{K}$ upon cooling. Hysteresis is observed, in that upon warming from the low-temperature (LT) phase to the HT phase, this transition occurs at a higher tempera-

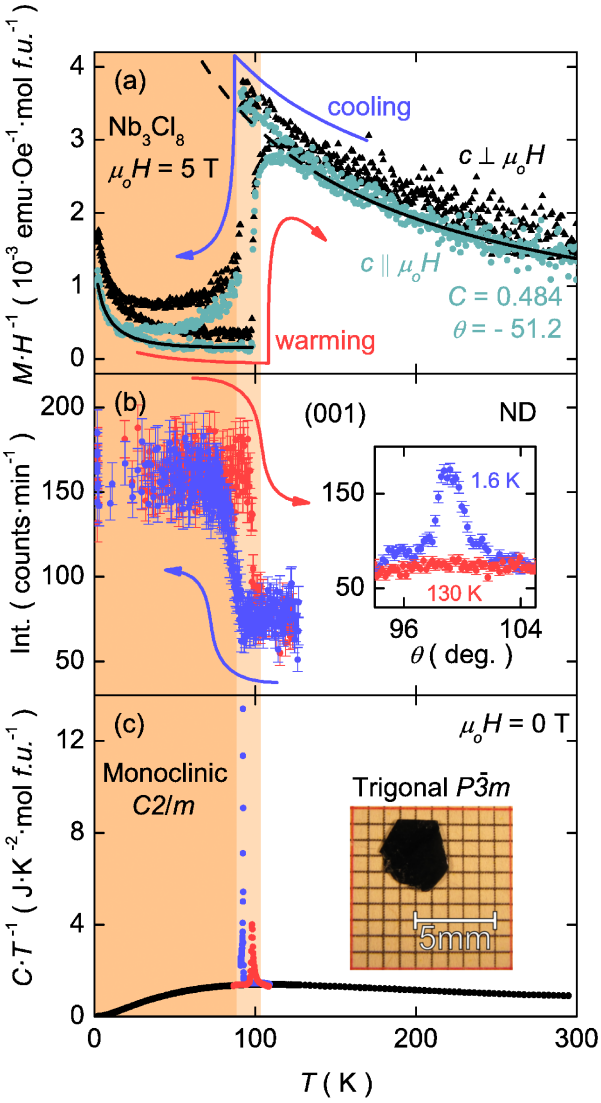

Figure 2 (a) Nb_3Cl_8 susceptibility with applied field parallel (∥) and perpendicular (⊥) to the crystallographic *c*-direction. Curie-Weiss fits to $c \parallel \mu_o H$ data is shown as a black line, for both high- and low-temperature regions. (b) Neutron diffraction (ND) intensity of the (001) reflection of Nb_3Cl_8, which grows upon entering the *C*2/*m* phase. The inset shows the (001) peak at T = 1.6 K and its absence at T = 130 K. (c) Heat capacity over temperature vs. temperature for Nb_3Cl_8. Peaks around $T \approx 100$ K are first-order heating and cooling transitions between the two phases. The inset shows a single crystal grown by vapor transport. The orange background corresponds to the LT *C*2/*m* monoclinic phase.

ture than upon cooling. An analysis of the inverse susceptibility data for $T > 140\,\mathrm{K}$ yields a Curie constant $C = 0.484\ \mathrm{emu \cdot K \cdot mol\, f.u.^{-1} \cdot Oe^{-1}}$ ($p_{eff} = 1.97$, consistent with $S_{eff} = 1/2$) and a Weiss temperature of $\theta = -51.2\,\mathrm{K}$. The fit is shown as a solid black line in Fig. 2 (a), for $140\,\mathrm{K} \leq T \leq 300\,\mathrm{K}$ and is continued as a dashed line at lower temperatures. The values vary less than 5% between the two crystal directions, indicating any HT anisotropy is small. The upturns observed below $T \approx 30\,\mathrm{K}$ account for ≈ 2% of the high-temperature spins, consistent with a small number of impurity spins or edge states. The fit shown below $T \approx 90\,\mathrm{K}$ in Fig. 2 (a) is to a Curie-Weiss law, $\chi = \frac{C}{T-\theta} + \chi_0$ where $\chi_0 = 0.8 \times 10^{-4}\ \mathrm{emu \cdot Oe^{-1} \cdot mol\ f.u.^{-1}}$ and $\theta = -4\,\mathrm{K}$.

Fig. 2 (b) shows the results of neutron diffraction rocking scans of the Nb_3Cl_8 (001) reflection. Compared to the HT phase, the LT phase has a significant increase in the intensity of the (001) reflection, which tracks the transition between the LT and HT phases, with consistent hysteresis.

Heat capacity measurements on Nb_3Cl_8 are shown in Fig. 2 (c). The cooling (blue) and warming (red) transitions are consistent with the susceptibility and diffraction data. The amount of entropy associated with the transitions is obtained from $S(T) = \int_0^T C_v \cdot T^{-1} dT$ assuming $C_v \approx C_p$, after a smooth curve to account for the background is subtracted. This results in an entropy change $\Delta S = 5\ \mathrm{J \cdot K^{-1} \cdot mol}\ f.u.^{-1}$, which is 85% of the full entropy change of a two level system, $R \cdot ln(2) = 5.76\ \mathrm{J \cdot K^{-1} \cdot mol}\ f.u.^{-1}$. This may suggest the bulk has a singlet ground state with a gap to the first excited state.

An analysis of the low temperature $C_P \cdot T^{-1}$ versus T^2 data (Fig. 3), however, reveals a significant linear contribution to the specific heat, indicative of metallic behavior, despite Nb_3Cl_8 being an insulator at all accessible temperatures. Measurements on two separate single crystal pieces yield two different linear contributions, $\gamma = 13$ and $18\ \mathrm{mJ \cdot K^{-2} \cdot mol}\ f.u.^{-1}$ for samples 1 and 2 respectively [Fig. 3 (a) and (b)]. The observation of varying values of the T-linear contribution to the specific heat suggests its origin is not intrinsic but rather due to defects that also give rise to the Curie tail in low temperature susceptibility data [Fig. 2 (a)]. To quantify this argument, the $C(T)$ data were fit to an equation accounting for the intrinsic sample behavior with a Schottky anomaly term for the low temperature impurity spins, $C \cdot T^{-1} = \beta \cdot T^2 + \gamma + (\frac{R}{T})(\frac{\Delta}{T})^2 \frac{e^{\Delta/T}}{[1+e^{\Delta/T}]^2}$, where γ is the T-linear contribution, β is the lattice contribution, R is the ideal gas constant, and Δ is the

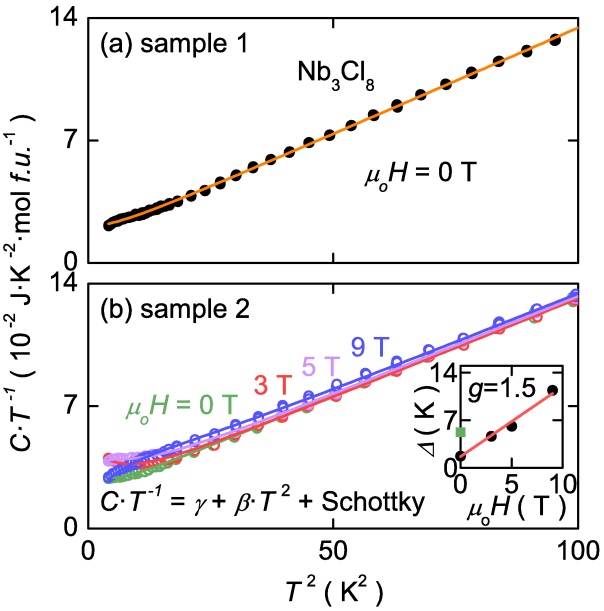

Figure 3 Low temperature $C_P \cdot T^{-1}$ versus T^2 data on two pieces (a,b) of the same batch of Nb_3Cl_8. Dots are data, lines are fits to the equation shown in (b). The values of γ extracted from fits to the data are $\approx 40\%$ different for the two pieces of Nb_3Cl_8 crystal, suggesting the origin of the T-linear component is from impurity spins. The inset in (b) shows the value of the Schottky gap as a function of field extracted from fits to data on sample 1 (green square) and sample 2 (black dots), which yield a g-factor of $1.5(1)$.

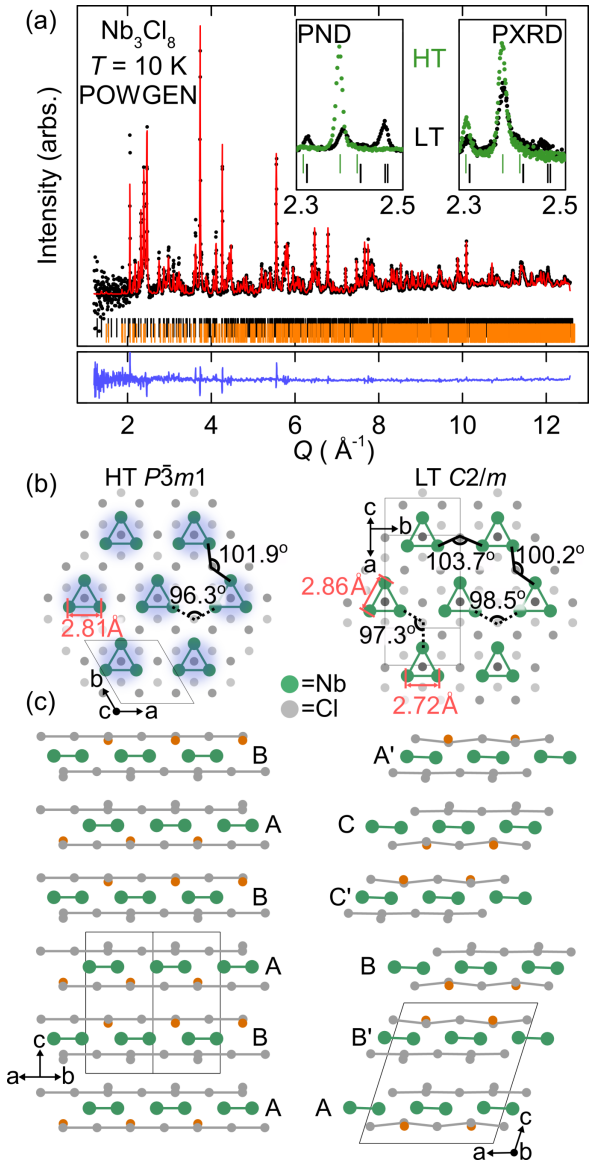

Figure 4 (a) Neutron diffraction at T = 10 K indicates LT-Nb_3Cl_8 adopts $C2/m$ space-group symmetry. Black dots are data, red line is calculated fit, blue line is difference, and tick marks are Bragg reflections for LT (black) and remnant HT (orange) phase Nb_3Cl_8. Insets show HT (green) and LT (black) data from neutron and X-ray diffraction at T = 10 K and T = 12 K, respectively, showing the split HT (202) trigonal reflection. HT and LT phase Nb_3Cl_8 structures are shown perpendicular (b) and parallel (c) to Nb_3Cl_8 layers. (b) Changes in intra-cluster Nb-Nb distances (red) and inter-cluster Nb-Cl-Nb bond angles (black) depict effect on intra-layer superexchange pathways. A shift in layer stacking (c) is observed from a HT -aaa- bilayer (-AB-AB- layer) to LT -abc- bilayer (-AB′-BC′-CA′- layer) order. Orange Cl atoms highlight puckering of Cl atom layers which drive closest packing and stacking order rearrangement.

Schottky anomaly gap. A single value of β and a single scale factor for the low temperature Schottky anomaly was used for all fields of sample 2 [Fig. 3 (b)]. The field dependence of the Schottky anomaly gap is shown in the inset to Fig. 3 (b), which is used to extract a g-factor of 1.5(1) for the impurity spins contributing to the anomaly. We thus reason the T-linear specific heat of Nb_3Cl_8 may originate from a distribution of broken singlets (giving rise to defect spins) that interact through the majority phase as in $Ba_3CuSb_2O_9$ [36] and Sr_2CuO_3 [37].

Table 1 Atomic parameters of LT-Nb_3Cl_8 from Rietveld refinement to neutron data at T = 10 K. The spacegroup is $C2/m$ with lattice parameters $a = 11.6576(1)$ Å, $b = 6.7261(1)$ Å, $c = 12.8452(1)$ Å and $\beta = 107.6087(2)^{o}$. All sites are fully occupied and thermal parameters were set equal for all atoms, with a refined value of $B_{iso} = 0.10(6)$. The fit quality is given by a $R_{wp} = 3.59$.

Atom	Wyck. site	x	y	z
Nb-1	4*i*	0.9734(10)	1/2	0.2470(10)
Nb-2	8*j*	0.1558(10)	0.2980(10)	0.2550(10)
Cl-1	4*i*	0.7046(10)	0	0.1231(10)
Cl-2	4*i*	0.2157(10)	0	0.1473(10)
Cl-3	4*i*	0.1271(10)	1/2	0.4013(10)
Cl-4	4*i*	0.1239(10)	0	0.3656(10)
Cl-5	8*j*	0.9595(10)	-0.2490(10)	0.1209(10)
Cl-6	8*j*	0.3725(10)	0.2606(10)	0.3622(10)

Low temperature powder X-ray and neutron diffraction was used to determine the LT structure. The LT phase has a characteristic pattern of peak splitting, indicating a structural distortion to a $C2/m$ phase. Rietveld refinement to neutron diffraction data at T = 10 K, shown in Fig. 4 (a), indicates a 16% remnant, random HT phase stacking pattern in the LT structure. The resulting structure is summarized in Table 1 and change in symmetry unique octahedral Nb-Cl bond lengths in Table 2. Considerable stacking faults and the remnant HT phase stacking present in the LT phase warranted use of FAULTS[32] to model the LT structure with all thermal parameters restrained to be equal to minimize refinable parameters and yield the most statistically significant model. The primary effect of the phase transition on the Nb_3Cl_{13} clusters is shown in Fig. 4 (b) and (c). The discrete Nb_3Cl_{13} clusters (2.81 Å intra- and 3.93 Å inter-cluster Nb-Nb bond distances) in the HT phase [Fig. 4 (b)] are characterized by "molecular" C_{3v} point group symmetry and a S_{eff} = 1/2 magnetic electron equally distributed over the entire cluster (blue shading). The clusters form a triangular lattice that are stacked in a -AB-AB- sequence. The transition to the LT phase [Fig. 4 (b) and (c)] results in removal of the threefold rotational symmetry of the HT clusters, so that only a $C2/m$ *a-c* mirror plane remains. The result is a scissoring of the clusters, whereby the HT phase equilateral Nb_3 triangular cluster becomes isosceles, resulting in one decreased (2.72 Å) and two increased (2.86 Å) Nb-Nb bond lengths and two inequivalent $NbCl_6$ octahedra, consistent with the SOJT effect. The transition modulates inter-cluster Nb-Cl-Nb superexchange pathways by decreasing and increasing these bond angles [Fig. 4 (b)] resulting in a pseudo-one-dimensional state. Further, accompanying the phase transition are changes to the nearest-neighbor (NN) inter- and intra-cluster distances, here defined as the distance between the geometric centroid of Nb_3 cluster triangles. While the intra-layer cluster distances are shorter and change from a single NN distance of 6.7457 Å (HT) to 6.7294 Å and 6.7261 Å (LT)—suggestive of 1D chains—the change in NN inter-layer distance is greater, from 7.3585 Å (HT) to 7.1887 Å (LT), consistent with inter-layer singlet formation. The cluster scissoring has a pronounced effect on the interlayer stacking arrangement. In the HT phase, Cl atoms at bilayer edges are flat triangular layers, resulting in a simple closest packing of chlorines from the top of one bilayer with the bottom of the next and thus, a -AB-AB- arrangement. In the LT phase, the

Table 2 Changes in the niobium-chlorine bond lengths of symmetry unique $NbCl_6$ octahedra in Nb_3Cl_{13} clusters between the HT and LT Nb_3Cl_8 phases. Bond lengths are separated and labeled by unique Cl atoms within an octahedra. Duplicate lengths within a $NbCl_6$ octahedra are labeled as such. Nb_A is the apical (*i.e.* non-scissored) Nb ion, Nb_B represent the two "scissored" Nb ions. All distances are in Angstroms (Å).

HT ($P3m1$)		**LT** ($C2/m$)	
Nb-Cl_A	2.437(2)	Nb_A-Cl_{A1}	2.483(13)
		Nb_B-Cl_{A2}	2.423(13)
Nb-Cl_B	$2 \times$ 2.530(1)	Nb_A-Cl_{B1}	$2 \times$ 2.552(11)
		Nb_B-Cl_{B2}	2.548(10)
		Nb_B-Cl_{B3}	2.497(13)
Nb-Cl_C	$2 \times$ 2.464(1)	Nb_A-Cl_{C1}	$2 \times$ 2.407(12)
		Nb_B-Cl_{C2}	2.435(12)
		Nb_B-Cl_{C3}	2.371(12)
Nb-Cl_D	2.640(1)	Nb_A-Cl_{D1}	2.513(13)
		Nb_B-Cl_{D2}	2.646(10)

scissoring motion results in a buckling of the chlorine layers as highlighted in Fig. 4 (c), where crystallographically equivalent orange Cl atoms emphasize the Cl-layer crimping distortion—the lowest interfacial energy between these now staggered layers requires a shift in stacking to a -AB′-BC′-CA′- pattern. Here, A/A′, B/B′, *etc* is used to relate the LT structure to the former HT (AB-designated) layers. The resultant shift in inter- and intra-layer structure, however, is not concomitant with long-range magnetic order. The observation of a structural distortion by powder X-ray diffraction suggests the increased intensity of (001) neutron Bragg diffraction [Fig. 2 (b)] has a structural—not magnetic—origin. Changes in the measured single crystal neutron diffraction data are consistent solely with nuclear diffraction associated with the $P\bar{3}m1$ to $C2/m$ phase transition.

Density functional theory (DFT) band structure calculations for Nb_3Cl_8, shown in Fig. 5, were used to gain insight into the nature of the magneto-structural transition. In agreement with previous calculations for discrete Nb_3Cl_{13} clusters[18], the HT Nb_3Cl_8 band structure confirms the highest occupied molecular orbital (HOMO) of each cluster is a non-degenerate a_1 orbital that is far in energy from the excited state orbitals and therefore, not conventionally (*i.e.* to first-order) Jahn-Teller active. The bands corresponding to each Nb_3Cl_{13} cluster HOMO [green and orange band, one from each of two clusters per unit cell, Fig. 5 (a)] are split at the Γ-point from orbital overlap between the magnetic electrons in adjacent clusters resulting in the formation of a bonding/anti-bonding pair of states. The band structure calculation of the LT phase, Fig. 5 (c), shows shifted bands with respect to the HT phase. Notably, the HT bonding/antibonding states [from Fig. 5 (a)] have an increased gap and the degenerate e states have been raised and lowered in energy (*i.e.* orbital degeneracy was broken) upon entering the LT phase. Breaking the degeneracy of the first excited states upon entering in the LT phase is consistent with a second-order Jahn-Teller distortion from orbital mixing. The calculations in Fig. 5 (a) and (c) have no spin-polarization (SP), spin-orbit coupling (SOC), or electronic interaction *via* a Hubbard U. Under these conditions, HT Nb_3Cl_8 is clearly predicted to have a finite density of

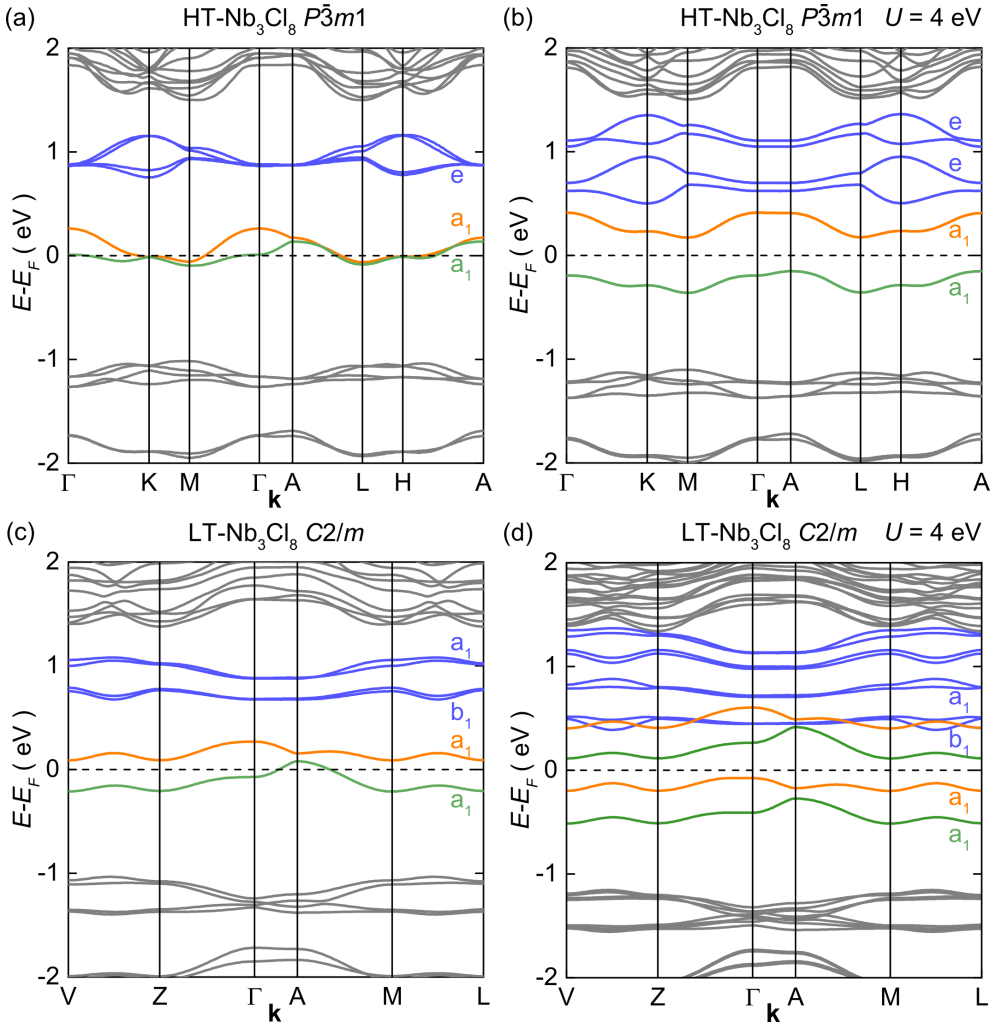

Figure 5 Band structure calculations on the HT [(a) and (b)] and LT [(c) and (d)] structures of Nb_3Cl_8. Calculations in (a) and (c) are performed without spin polarization (SP), spin-orbit coupling (SOC), or a Hubbard U. Calculations in (b) and (d) are performed with SP, SOC, and Hubbard $U = 4$ eV. The transition observed in Nb_3Cl_8 is driven by a second-order Jahn-Teller distortion driven by interaction of (a) HT phase e (blue) and a_1 orbitals. The HT phase possesses a bonding (green) and anti-bonding (orange) pair of states from the non-degenerate (a_1) valence bands at the Γ- point from an interaction between interlayer clusters. The HT phase e orbitals are split upon transition into the (c) LT state. To reproduce the experimentally observed insulating behavior in the HT calculation, the Hubbard U and SOC must be included (b), which splits both the non-degenerate a_1 and e bands. For comparison, inclusion of a Hubbard U in the LT calculations is shown in (d) (see ESI†). The special points of the Brillouin zone in both the HT and LT calculations are listed in the ESI†.

states at the Fermi level and thus be metallic, inconsistent with resistivity measurements. This demonstrates the importance of correlations in producing the observed behavior of this compound. Intriguingly, we find that solely SOC or solely a Hubbard U (onsite electron-electron interaction), are not sufficient to produce an insulator in the HT phase (see ESI†). Including both SOC and U simultaneously, Fig. 5 (b), is sufficient to produce an insulator. In this calculation, Nb moments were assumed to align with the crystallographic c axis, and be oriented antiferromagnetically between layers with a total moment of $\approx 0.5\,\mu_B$ per cluster in the HT phase. Given the limitations of DFT in describing correlated materials, this semi-quantitative agreement is reasonable. In contrast, LT Nb_3Cl_8 is almost predicted to be insulating by DFT, even in the absence of

SOC and a Hubbard U, Fig. 5 (c). This demonstrates the importance of changes in interlayer interactions, as the splitting of the HT a_1 bands induces the SOJT effect, driving this material toward an insulating state [of course inclusion of SOC and U increase the insulating gap, Fig. 5 (d)].

4 Discussion

The data demonstrate a first-order phase transition from a triangular lattice paramagnet with antiferromagnetic correlations to a non-magnetic state. The transition temperature $T \approx 90\,\mathrm{K}$ is higher than the Weiss temperature (θ), a measure of the magnetic interaction strength. Typically a material, absent of any magnetic frustration effects, will form a magnetically long-range ordered state with $T_{order} = |\theta|$, with the kind of ordering (ferro- or antiferromagnetic) dependent on the sign of the Weiss temperature. In Nb_3Cl_8, the onset of the SOJT effect well above the temperature at which in-plane magnetic correlations become strong suggests an inherent instability of the system. The effects of magnetic frustration observed in another triangular lattice cluster-magnet based material, $LiZn_2Mo_3O_8$ [10–12,15], is proposed to result from itinerant, plaquette charge order [14] that does not form a long-range ordered state. In $LiZn_2Mo_3O_8$, as opposed to Nb_3Cl_8, stability of the frustrated magnetic state can be due to the non-magnetic Li/Zn ions suppressing inter-layer magnetic interactions predicted by band structure calculations (Fig. 5). In addition, previous reports suggest the Nb-Cl bonding within Nb_3Cl_{13} clusters has strong ionic character [17] as opposed to highly covalent bonding, which might give insight into the lack of stability of the frustrated magnetic state—the ionic character of the cluster bonds is more susceptible to a SOJT effect and subsequent structural distortion due to the low energy barrier to overcome.

We compare the peculiar structural distortion observed in Nb_3Cl_8 with other anomalous magnetism in materials and 2D VdW structures. It has been suggested that the observed properties of the triangular lattice antiferromagnet $NaTiO_2$ [22] can be explained by a one-dimensional-like behavior [38,39] arising from a symmetry lowering structural distortion, where energetically similar orbitals are thermally populated at high temperatures, Fig. 6 (a). Upon cooling, a distortion relieves the frustration by orbital ordering of the Ti^{3+} cations to form 1D chains, Fig. 6 (b). Analogous behavior is observed in other compounds with single ions as the basic magnetic unit, including $NaVO_2$ [24] and $LiVO_2$ [40]. A similar phenomenology is found in cluster-based Lacunar spinels such as $GaNb_4S_8$ [41]. There, a first-order Jahn-Teller distortion due to a single electron in a t_{2g} triply degenerate orbital set, Fig. 6 (c), results in the localization of the unpaired electron on a single Nb atom in the Nb_4S_4 cores, Fig. 6 (d). This ordering is concomitant with a drop in magnetism, thought to result from the formation of spin-singlets between two clusters [42] *via* interaction of adjacent-cluster Nb atoms [Fig 6 (d)]. Singlet formation born from orbital ordering is also seen in other potentially frustrated systems such as $Ba_3CuSb_2O_9$ [43] and $Ba_3CoSb_2O_9$ [44]. In all of these cases, the orbital degree of freedom plays a crucial role in driving the structural distortion that relieves magnetic frustration and results in either magnetic order

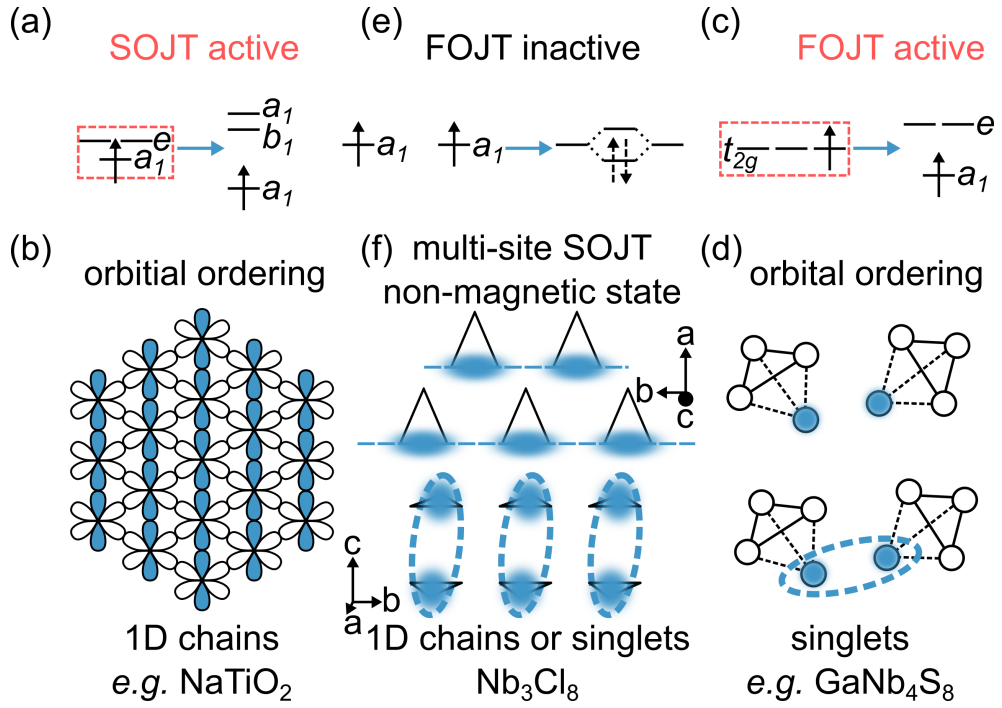

Figure 6 Subtle electronic and magnetic interactions can cause materials to avoid frustration. Simplified band pictures show Jahn-Teller (JT) active distortions upon entering low temperature phases in (a) $NaTiO_2$ and (c) $GaNb_4S_8$. (e) The HT phase of Nb_3Cl_8 has a multi-site interaction between a_1 orbitals on adjacent, inter-layer Nb_3Cl_{13} clusters. The distortion to the LT phase is driven by a SOJT effect, despite the $\approx$ 1 eV energy gap, and thus, vanishingly small thermal population of the degenerate e orbitals. Magnetic order in various materials is achieved (b) by the formation of 1D chains (in plane Ti-d orbitals shown) *via* orbital ordering (OO) in $NaTiO_2$, (d) OO and singlet formation in $GaNb_4S_8$. Further neutron scattering experiments are required to determine either (f) 1D chains or singlets as the magnetic ground state in Nb_3Cl_8.

or a singlet state.

Nb_3Cl_8 exhibits similar physics despite the absence of an orbital degeneracy (*i.e.* first-order Jahn-Teller instability) or significant thermal population of the first excited state. The results of band structure calculations on LT-Nb_3Cl_8 [Fig. 5 (c)] indicate second-order Jahn-Teller (SOJT) like orbital mixing, since upon entering the LT state, HT degenerate e bands [blue bands, Fig. 5 (a)] break their degeneracy and a scissoring of the Nb_3 triangles is expected from the SOJT effect. This is surprising given the $\approx$ 1 eV energy gap to the degenerate e states in the HT band structure, which are expected to have little-to-no thermal population at $T \approx 90$ K. The HT band structure calculation predicts an electronic interaction by orbital overlap between magnetic electrons in adjacent Nb_3Cl_8 layers—yielding effective bonding/antibonding states—possibly inducing the SOJT effect and is suggestive of an inter-layer singlet ground state in the LT phase. Such a singlet ground state would be highly unusual given the large distance between Nb ions in adjacent layers, although magnetic exchange interactions are possible on such length scales, as in α-$RuCl_3$ [45–47], which harbors an out of plane magnetic interaction and similar stacking faults as LT Nb_3Cl_8. Alternatively, the concurrent change in intra-layer, inter-cluster Nb-Cl-Nb bond angles upon entering the LT phase could result in a intra-layer $S_{eff} = 1/2$ 1D chain singlet state. While at present, the LT magnetic ground state cannot be unambiguously

determined, singlets that lie in between adjacent layers or a intra-layer $S_{eff} = 1/2$ 1D chain appear to be the most likely candidates. Indeed, while no in-plane dimerization is observed, dimerization *via* electronic interaction in the *c*-direction exists even in the HT phase.

The DFT calculations affirm the HOMO in each HT Nb_3Cl_{13} cluster are non-degenerate (a_1), so the transition in Nb_3Cl_8 cannot be ascribed solely to single-site orbital ordering. Related phenomena are observed in two-dimensional organic salts where charge ordering is the cause of the metal-insulator transition as in θ-(BEDT-TTF)$_2$RbZn(SCN)$_4$[48]. The observation of a dielectric response in the geometrically frustrated dimer Mott insulator κ-(BEDT-TTF)$_2$Cu$_2$(CN)$_2$[49] suggests charge order plays a role in the putative spin liquid state. Devoid of a screw-axis, the HT $P\bar{3}m1$ space group is symmorphic, and therefore the formation of a gapped, trivial magnetic ground state is allowed without a structural distortion in Nb_3Cl_8[50,51]. Instead, the observation of the SOJT effect and subsequent non-magnetic ground state in the presence of non-degenerate HOMO bands and unpopulated degenerate *e* bands reveals that the electronic interaction [Fig. 6 (e)] due to orbital overlap plays a crucial role in the avoidance of a magnetically frustrated, classically degenerate ground state. Estimates of the change in entropy and enthalpy from the specific heat measurements in Fig. 2 (c) suggest the first-order transition is entropically driven, by the enhanced spin entropy of the frustrated magnetic HT phase over that of a supposed spin singlet LT phase. The apparent lack of long-range magnetic order in LT-Nb_3Cl_8 is a natural consequence of the two likely magnetic ground state scenarios—formation of a spin-ladder network of inter-layer singlets or intra-layer 1D chains, illustrated in Fig. 6 (f). The first-order nature of the transition prevents estimation of the low temperature magnetic exchange interactions (*e.g.* the magnitude of the spin gap) based on the HT phase properties. The deeply suppressed magnetic response in the LT phase implies a gap in the LT state, $\Delta \approx 150 - 650\,\mathrm{K}$ (see ESI†), that is significantly larger than the HT Weiss temperature, but not inconsistent with the $\approx 200\,\mathrm{meV}$ splitting of the a_1 orbitals at the Γ-point in the DFT calculations. Further spectroscopic investigations, such as inelastic neutron scattering, are required to elucidate the exact nature of the LT magnetic ground state.

Lastly, the discovery of extraordinary physical properties of graphene[52,53] and other 2D VdW materials—such as transition metal dichalcogenides[54–57]—has prompted materials scientists to feverishly search for new systems with properties suitable to, *e.g.*, fabricate technologically useful devices. Like Nb_3Cl_8, these materials are (strongly) covalently bonded in two dimensions while adhesion in the third dimension is controlled by comparatively weak VdW forces. This weak bonding in one dimension allows for unparalleled control over heterostructure fabrication possibilities due to the facile nature by which differing interlayers can be combined[58,59] to create nano-scale electronic devices such as precisely tunable transistors[60,61] or LEDs[62]. Nb_3Cl_8 is a rare example of a material, despite its absence of "molecular" (Nb_3Cl_{13}) HOMO degeneracy and energetically isolated HOMO bands, that undergoes a rearrangement of layer stacking at low temperature due to inter-layer magnetic interactions. Our insight gained into the SOJT-like effect in Nb_3Cl_8, which drives

the puckering of interfacial VdW Cl layers and forces the shift in stacking arrangement, opens up possibilities for low-temperature device applications where controllable structural changes are desired. The ability for interactions in the VdW-layer-direction to control crystal structure can be combined with other 2D VdW layers to create novel devices.

5 Conclusions

In short, Nb_3Cl_8 highlights the interplay between charge, orbital, and spin degrees of freedom and the approach to a non-entropic state as $T \to 0$. While the space group symmetry does not preclude a singlet ground state in the symmorphic high temperature structure with two valence electrons[63,64], such a state is apparently not energetically favorable. At low temperature, on the other hand, the strongly reduced susceptibility and inter-layer HOMO overlap suggested by DFT point to a singlet ground state of the valence bond crystal variety. While the structural transition must be energetically favorable for low-T magnetism, the second-order Jahn-Teller driven structural rearrangement must be costly. The transition is thus analogous to a spin-Peierls transition where an energetically unfavorable structural dimerization is induced to lift spin degeneracy. For Nb_3Cl_8, a preference to avoid frustrated triangular lattice antiferromagnetism may even drive covalent bonding. Unheard of in conventional local moment magnetism, this scenario may not be uncommon for 4d or 5d magnetic materials, and has recently been proposed as an explanation for the behavior of Li_2RuO_3 and related iridium-based materials[65]. More generally, that such a change in stacking of a Van-der-Waals material can occur near liquid nitrogen temperature is remarkable, and implies that designer 2-D heterostructures may be engineered to undergo similar phase transitions for a variety of potential applications. Akin to the wide breadth of physical phenomena discovered in graphene, the Van-der-Waals layered structure of Nb_3Cl_8 may also yield novel physics as the first mono-layer geometrically frustrated magnet.

6 Acknowledgements

This research was supported by the US Department of Energy, Office of Basic Energy Sciences, Division of Materials Sciences and Engineering under Award DE-FG02-08ER46544 to The Institute for Quantum Matter at JHU. Use of the Advanced Photon Source at Argonne National Laboratory was supported by the U. S. Department of Energy, Office of Science, Office of Basic Energy Sciences, under Contract No. DE-AC02-06CH11357. Utilization of the mail-in program at POWGEN, Spallation Neutron Source, ORNL was sponsored by the Scientific User Facilities Division, Office of Basic Energy Sciences, U.S. Department of Energy. TMM acknowledges support from the David and Lucile Packard Foundation and the Sloan Research Fellowship. The authors would like to thank O. Tchernyshyov and A. Turner for useful discussions, L. Harriger for his support on the SPINS spectrometer, and S. Lapidus for his support on beamline 11-BM.

Supplementary Information:

Rearrangement of Van-der-Waals Stacking and Formation of a Singlet State at $T = 90\,\mathrm{K}$ in a Cluster Magnet

John P. Sheckelton,[a,b] Kemp W. Plumb,[b] Benjamin A. Trump,[a,b] Collin L. Broholm,[b,c,d] and Tyrel M. McQueen[a,b,c,*]

S1 Synchrotron powder diffraction analysis

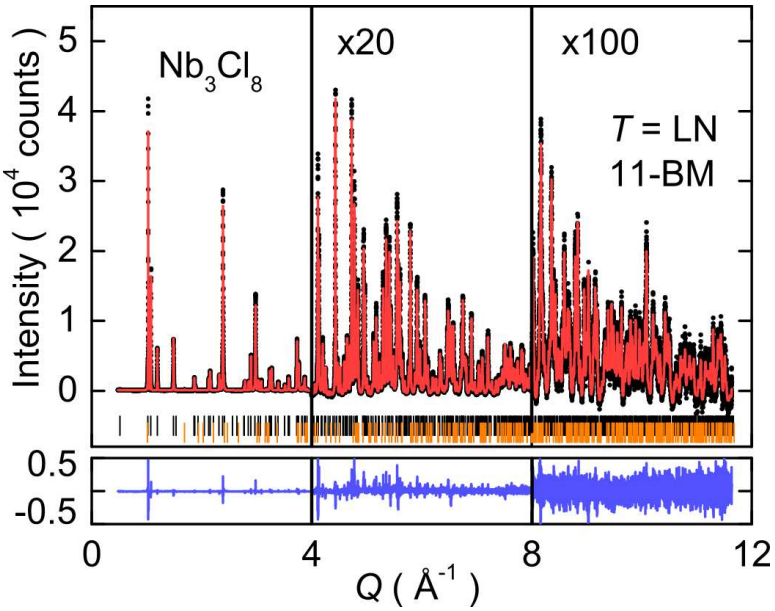

Figure S1 Nb_3Cl_8 Rietveld analysis of synchrotron X-ray diffraction data at liquid nitrogen (LN) temperatures. Black dots are data, red line is the calculated fit, blue line is the difference, tick marks are Bragg reflections for Nb_3Cl_8 (black) and a minor impurity, $NbOCl_2$ (orange, 0.5(2) wt%). The higher Q data are multiplied $\times 20$ ($4 \geq Q \geq 8$) and $\times 100$ ($8 \geq Q \geq 12$) to highlight the quality of the fit.

Table S1 is a summary of Rietveld refinement parameters to $T = 300\,\mathrm{K}$ synchrotron X-ray powder diffraction data shown in main text Fig. 1(a). Low temperature synchrotron X-ray powder diffraction data near liquid nitrogen temperatures shows no signs of symmetry lowering distortions despite a temperature reading of approximately 80 K near the sample. Rietveld refinement of the HT ($P\bar{3}m1$) structure to the data near liquid nitrogen temperatures is shown in Fig. S1 and is summarized in Table S2. 80 K is far below the first-order phase transition in Nb_3Cl_8 ($\approx 90\,\mathrm{K}$)—the absence of any Nb_3Cl_8 LT phase, therefore, is attributed to sample heating from the 30 KeV ($\lambda \approx 0.41\,\text{Å}$) incident X-ray beam. As is the case with the $T = 300\,\mathrm{K}$ data, fitting the low temperature data to lower symmetry models ($P\bar{3}$, $P3m$, $P3$, and $C2/m$) results in no improvement of the

Table S1 Nb_3Cl_8 Rietveld refinement to synchrotron X-ray ($\lambda = 0.4132$ Å) powder diffraction data at T = 300 K, shown in main text Fig. 1(a). The spacegroup is $P\bar{3}m1$ (164) with lattice parameters $a = 6.74566(3)$ Å, $c = 12.28056(7)$ Å, $\alpha = \beta = 90^o$, and $\gamma = 120^o$. All sites are fully occupied, cell volume was calculated to be $V = 483.947(6)$ Å^3, and atomic displacement parameters were freely refined for all atoms. The fit quality is given by $R_{wp} = 11.34\%$, $R_p = 9.03\%$, and $\chi^2 = 3.286$. Errors are computed statistical uncertainties.

Atom	Wyckoff position	x	y	z	U_{iso}(Å^2)
Nb	6*i*	0.52763(2)	0.05525(5)	0.24577(5)	0.00473(6)
Cl-1	2*d*	2/3	1/3	0.0978(2)	0.0045(4)
Cl-2	2*d*	1/3	2/3	0.3555(2)	0.0085(5)
Cl-3	6*i*	0.6696(2)	-0.1652(1)	0.1350(1)	0.0069(3)
Cl-4	6*i*	0.3374(2)	0.1687(1)	0.3835(1)	0.0103(3)

Table S2 Nb_3Cl_8 Rietveld refinement to synchrotron X-ray ($\lambda = 0.4132$ Å) powder diffraction data at $T \approx 90$ K, shown in Fig. S1. The spacegroup is $P\bar{3}m1$ (164) with lattice parameters $a = 6.73255(2)$ Å, $c = 12.22222(5)$ Å, $\alpha = \beta = 90^o$, and $\gamma = 120^o$. All sites are fully occupied, cell volume was calculated to be $V = 479.777(4)$ Å^3, and atomic displacement parameters were freely refined for all atoms. The fit quality is given by $R_{wp} = 9.31\%$, $R_p = 7.61\%$, and $\chi^2 = 2.141$. Errors are computed statistical uncertainties.

Atom	Wyckoff position	x	y	z	U_{iso}(Å^2)
Nb	6*i*	0.52746(2)	0.05493(4)	0.24622(4)	0.00182(4)
Cl-1	2*d*	2/3	1/3	0.0981(2)	0.0024(3)
Cl-2	2*d*	1/3	2/3	0.3560(1)	0.0041(3)
Cl-3	6*i*	0.6709(1)	-0.16456(6)	0.13528(7)	0.0023(2)
Cl-4	6*i*	0.3359(1)	0.16793(6)	0.38192(8)	0.0051(2)

fit, either quantitatively or qualitatively.

S2 DFT band structure calculations

Calculations on the high temperature (HT) structure of Nb_3Cl_8 were performed without spin-polarization [Fig. S2 (a)], with spin-polarization [Fig. S2 (b)], with spin-orbit coupling [Fig. S2 (c)], and with a Hubbard U term [Fig. S2 (d)], all of which display the same qualitative highest occupied molecular orbital (HOMO) splitting at the Γ point as in Fig. S2 (a). The calculations in Fig. S2 (b)-(d) have an additional splitting of the HOMO bands over the entire Brillouin zone originating from the formation of antiferromagnetic order between ferromagnetic planes. The onset of antiferromagnetic order in Fig. S2 (b)-(d) stems from the initial application of a magnetic field to split spin degeneracy despite a reduction of the applied field with subsequent calculation iterations and a convergence with no applied field. The application of a Hubbard U, Fig. S2 (d), is required to fully open the gap and predict insulating behavior. The splitting observed in the a_1 derived bands in these calculations is allowed due to the unit cell symmetry and there being an even number of electrons per unit cell[63]. The large cluster interaction energy indicated by the width of the a_1 band (≈ 200 meV) clearly plays a key role in the collective transition from a triangular lattice $S_{eff} = 1/2$ antiferromagnet to a system of static singlets.

The special points of the Brillouin zone used in the HT phase calculations are for a trigonal unit cell in the hexagonal setting and are Γ = (000), K = $(\frac{\bar{1}}{3}\frac{2}{3}0)$, M = $(0\frac{1}{2}0)$, A = $(00\frac{1}{2})$, L = $(0\frac{1}{2}\frac{1}{2})$, and H = $(\frac{\bar{1}}{3}\frac{2}{3}\frac{1}{2})$. The

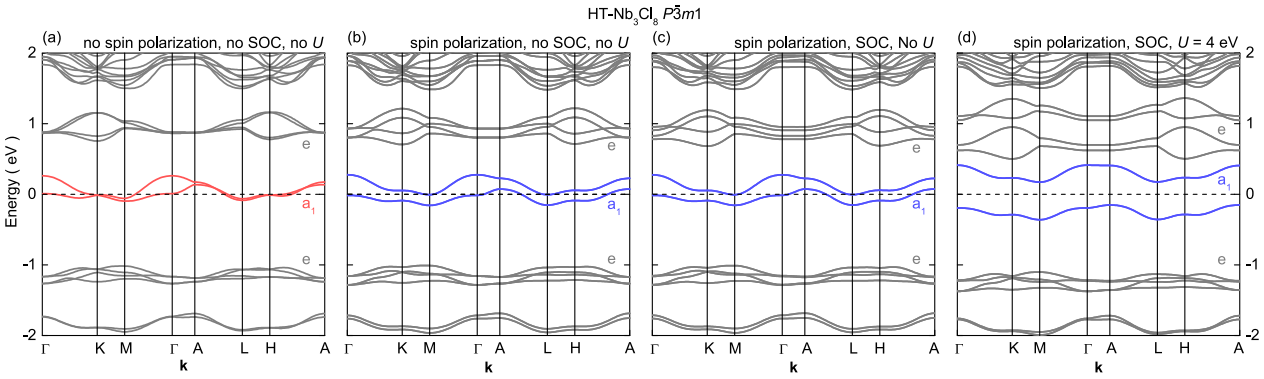

Figure S2 Band structure calculations on HT-Nb_3Cl_8 with (a) no spin polarization (SP), spin-orbit coupling (SOC), or Hubbard U, (b) SP but no SOC/U (c) SP and SOC but no U, and (d) SP, SOC, and $U = 4$ eV. The red highlighted bands in (a) are the highest occupied a_1 orbitals, which are split at the Γ-point from the formation of a bonding/anti-bonding pair and are far in energy (≈ 1 eV) from the degenerate e orbitals. In (b)-(d), the total splitting of the a_1 band (blue) is due to antiferromagnetic order. The spin polarized calculations are initiated with the application of an applied field to break spin degeneracy. This results in calculations (b)-(d) converging with antiferromagnetic order where Nb_3Cl_{13} cluster spins are oriented in the crystallographic c-axis. In (d), the antiferromagnetic band splitting is exacerbated by the electronic interaction induced by the Hubbard U.

special points of the Brillouin zone for a monoclinic unit cell in the $C2/m$ space group with unique axis b, cell choice 1 used in the LT calculations are $\mathrm{V} = (\frac{1}{2}00)$ $\mathrm{Z} = (\frac{1}{2}\frac{1}{2}0)$ $\Gamma = (000)$ $\mathrm{A} = (00\frac{1}{2})$ $\mathrm{M} = (\frac{1}{2}\frac{1}{2}\frac{1}{2})$ $\mathrm{L} = (\frac{1}{2}0\frac{1}{2})$.

S3 Spin-Peierls analysis

The transition into a spin-Peierls (SP) state is marked by an exponential decay of the magnetic susceptibility as a function of temperature[66]. The SP transition temperature depends on the magnetic interaction strength and the spin excitation gap in the SP state. Nb_3Cl_8 does not have an exponential decay into the low-temperature (LT) state—the first-order nature of the transition results in remnant domains of the HT phase upon cooling. Instead, a plot of magnetic susceptibility collected upon warming, Fig. S3, of the $c \parallel \mu_o H =$ data [reproduced from main text Fig. 2 (a)] must be used in modeling the behavior of the bulk LT state. As can be seen in Fig. S3, the susceptibility data is flat in temperature (with the exception of the Curie tail in $T \leq 50$ K) up to the transition at $T \approx 100$ K. To test that the magnetic susceptibility from a SP state (χ_{SP}) is varying minimally with temperature, a Curie-Weiss fit to the LT data up to $T = 50$ K and $T = 100$ K was performed to extract a value of $\chi_{\mathrm{o}} \approx \chi_{\mathrm{SP}}$ for the two temperature regions, a deconvolution of the Curie tail contribution. Values of $\chi_{\mathrm{o}} = 0.8$ and 0.7×10^{-4} emu $\cdot$ Oe^{-1} $\cdot$ mol $f.u.^{-1}$ are extracted for fits up to $T = 100$ K and $T = 50$ K respectively.

The magnetic behavior of a SP state can be approximated by the exponential[67]

$$\chi_m = C\, e^{\frac{-2\Delta}{k_B T}} + \chi_{\mathrm{o}}$$

where χ_m is the molar susceptibility, C is the Curie constant, 2Δ is the gap to the first excited state, k_B is Boltzmann's constant, and χ_{o} is the temperature independent contribution to the susceptibility. It is im-

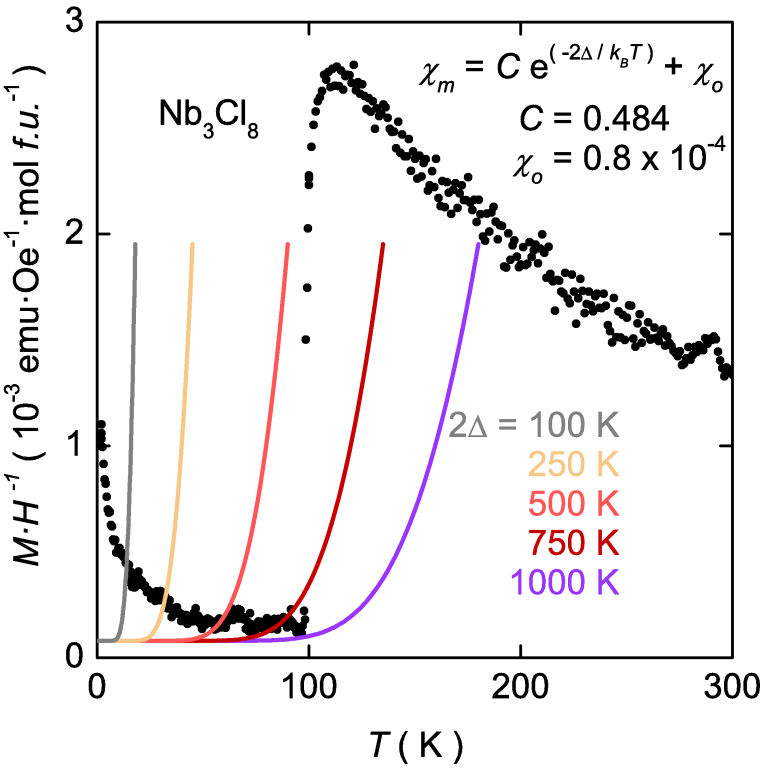

Figure S3 Nb_3Cl_8 magnetic susceptibility data (black dots) as a function of temperature upon warming. The data at LT is a convolution of a Curie tail and the intrinsic behavior of the LT magnetic state of Nb_3Cl_8. The colored lines are calculations of the exponential behavior expected of a spin-Peierls state. As can be seen, a gap of at least $2\Delta = 1000\,\mathrm{K}$ must exist in order to observe the magnetic behavior of a spin-Peierls state in Nb_3Cl_8.

portant to note that the transition temperature between HT and LT states in Nb_3Cl_8 is not necessarily the spin-Peierls transition—since the transition in Nb_3Cl_8 is first-order, the HT and LT magnetic behaviors need not be related in any way. Assuming the LT state in Nb_3Cl_8 is a SP state, then calculations for various magnitudes of the spin gap show that the gap must be at least $2\Delta = 1000\,\mathrm{K}$ in order reproduce the observed behavior. These calculations assume the Curie constant is the value extracted from the HT fit for a $S_{eff} = 1/2$ system, $C = 0.484\ \mathrm{emu \cdot K \cdot mol}\, f.u.^{-1} \cdot \mathrm{Oe}^{-1}$, and the temperature independent contribution is $\chi_o = 0.8 \times 10^{-4}\ \mathrm{emu \cdot Oe^{-1} \cdot mol}\ f.u.^{-1}$.

The magnitude of the spin gap may also be estimated, assuming LT Nb_3Cl_8 is a spin-Peierls state and the transition temperature $T_c = 100\,\mathrm{K}$, by examining the ratio of the susceptibility above and below the transition as is done in other SP materials such as $CuGeO_3$[26]. Approximating $\chi_{\mathrm{HT}}/\chi_{\mathrm{LT}} \approx R$, and rearranging $R = e^{\frac{-\Delta}{T_c}}$ to $\Delta = T_c \cdot ln(R)$ with $R \approx 30$ gives $\Delta = 100\,\mathrm{K} \cdot ln(30) = 340\,\mathrm{K}$. This is on the same order as to what may be expected of a SP system, where the gap $\Delta \approx 1.5 \cdot T_c$.

We can also make an approximation of the exchange constant J in the Nb_3Cl_8 spin-Peierls system from the spin-phonon coupling constant given by Cross and Fisher[68]. Here, $T_c = 0.8 \cdot J \cdot \eta$, or $J = \frac{T_c \cdot 1.25}{\eta}$. Assuming the value of η used for $CuGeO_3$, $\eta = 0.2$, is used for Nb_3Cl_8, the calculation yields a $J = \frac{100\,\mathrm{K} \cdot 1.25}{0.2} = 625\,\mathrm{K}$—much larger than the value extracted from the Curie-Weiss fit to the HT susceptibility data of $\theta = 51.2\,\mathrm{K}$.

This discrepancy may be indicative of a strong enhancement of the exchange constants upon entering the LT state from the structural rearrangement, or that a spin-Peierls model fails to adequately explain the magnetic behavior of Nb_3Cl_8.

References

[1] M. Rotter, M. Tegel and D. Johrendt, *Physical Review Letters*, 2008, **101**, 107006.

[2] E. H. d. S. Neto, P. Aynajian, A. Frano, R. Comin, E. Schierle, E. Weschke, A. Gyenis, J. Wen, J. Schneeloch, Z. Xu, S. Ono, G. Gu, M. L. Tacon and A. Yazdani, *Science*, 2014, **343**, 393–396.

[3] J. Nagamatsu, N. Nakagawa, T. Muranaka, Y. Zenitani and J. Akimitsu, *Nature*, 2001, **410**, 63–64.

[4] D. E. Moncton, J. D. Axe and F. J. DiSalvo, *Physical Review B*, 1977, **16**, 801–819.

[5] Y. L. Chen, J. G. Analytis, J.-H. Chu, Z. K. Liu, S.-K. Mo, X. L. Qi, H. J. Zhang, D. H. Lu, X. Dai, Z. Fang, S. C. Zhang, I. R. Fisher, Z. Hussain and Z.-X. Shen, *Science*, 2009, **325**, 178–181.

[6] D. Hsieh, Y. Xia, D. Qian, L. Wray, F. Meier, J. H. Dil, J. Osterwalder, L. Patthey, A. V. Fedorov, H. Lin, A. Bansil, D. Grauer, Y. S. Hor, R. J. Cava and M. Z. Hasan, *Physical Review Letters*, 2009, **103**, 146401.

[7] F. Iga, N. Shimizu and T. Takabatake, *Journal of Magnetism and Magnetic Materials*, 1998, **177**, 337–338.

[8] T. E. Mason, G. Aeppli, A. P. Ramirez, K. N. Clausen, C. Broholm, N. Stucheli, E. Bucher and T. T. M. Palstra, *Physical Review Letters*, 1992, **69**, 490–493.

[9] T. T. M. Palstra, A. A. Menovsky, J. van den Berg, A. J. Dirkmaat, P. H. Kes, G. J. Nieuwenhuys and J. A. Mydosh, *Physical Review Letters*, 1985, **55**, 2727–2730.

[10] J. P. Sheckelton, J. R. Neilson, D. G. Soltan and T. M. McQueen, *Nature Materials*, 2012, **11**, 493–496.

[11] J. P. Sheckelton, F. R. Foronda, L. D. Pan, C. Moir, R. D. McDonald, T. Lancaster, P. J. Baker, N. P. Armitage, T. Imai, S. J. Blundell and T. M. McQueen, *Physical Review B*, 2014, **89**, 064407.

[12] J. P. Sheckelton, J. R. Neilson and T. M. McQueen, *Materials Horizons*, 2014.

[13] R. Flint and P. A. Lee, *Physical Review Letters*, 2013, **111**, 217201.

[14] G. Chen, H.-Y. Kee and Y. B. Kim, *arXiv:1408.1963*.

[15] M. Mourigal, W. T. Fuhrman, J. P. Sheckelton, A. Wartelle, J. A. Rodriguez-Rivera, D. L. Abernathy, T. M. McQueen and C. L. Broholm, *Physical Review Letters*, 2014, **112**, 027202.

[16] J. R. Kennedy and A. Simon, *Inorganic Chemistry*, 1991, **30**, 2564–2567.

[17] J. R. Kennedy, P. Adler, R. Dronskowski and A. Simon, *Inorganic Chemistry*, 1996, **35**, 2276–2282.

[18] G. J. Miller, *Journal of Alloys and Compounds*, 1995, **217**, 5–12.

[19] H.-G. v. Schnering, H. Wöhrle and H. Schäfer, *Naturwissenschaften*, 1961, **48**, 159–159.

[20] F. A. Cotton, M. P. Diebold, X. Feng and W. J. Roth, *Inorganic Chemistry*, 1988, **27**, 3413–3421.

[21] J. Kennedy and A. Simon, *Materials Science Forum*, 1992, **91-93**, 183–188.

[22] S. J. Clarke, A. J. Fowkes, A. Harrison, R. M. Ibberson and M. J. Rosseinsky, *Chemistry of Materials*, 1998, **10**, 372–384.

[23] S. Y. Ezhov, V. I. Anisimov, H. F. Pen, D. I. Khomskii and G. A. Sawatzky, *Europhysics Letters*, 1998, **44**, 491.

[24] T. M. McQueen, P. W. Stephens, Q. Huang, T. Klimczuk, F. Ronning and R. J. Cava, *Physical Review Letters*, 2008, **101**, 166402.

[25] S. Jakob, H. Müller, D. Johrendt, S. Altmannshofer, W. Scherer, S. Rayaprol and R. Pöttgen, *Journal of Materials Chemistry*, 2007, **17**, 3833–3838.

[26] M. Hase, I. Terasaki and K. Uchinokura, *Physical Review Letters*, 1993, **70**, 3651–3654.

[27] M. Isobe, E. Ninomiya, A. N. Vasil'ev and Y. Ueda, *Journal of the Physical Society of Japan*, 2002, **71**, 1423–1426.

[28] M. Shaz, S. van Smaalen, L. Palatinus, M. Hoinkis, M. Klemm, S. Horn and R. Claessen, *Physical Review B*, 2005, **71**, 100405.

[29] S. van Smaalen, L. Palatinus and A. Schönleber, *Physical Review B*, 2005, **72**, 020105.

[30] A. Seidel, C. A. Marianetti, F. C. Chou, G. Ceder and P. A. Lee, *Physical Review B*, 2003, **67**, 020405.

[31] M. W. Schmidt, K. K. Baldridge, J. A. Boatz, S. T. Elbert, M. S. Gordon, J. H. Jensen, S. Koseki, N. Matsunaga, K. A. Nguyen, S. Su, T. L. Windus, M. Dupuis and J. A. Montgomery, *Journal of Computational Chemistry*, 1993, **14**, 1347–1363.

[32] M. Casas-Cabanas, J. Rodríguez-Carvajal and M. Palacín, *Zeitschrift für Kristallographie, Suppl*, 2006, **23**, 243–248.

[33] *Physical Properties Measurement System: Hardware Manual, Quantum Design*, 2009.

[34] *Available under the GNU General Public License at elk.sourceforge.net*.

[35] M. Ströbele, J. Glaser, A. Lachgar and H.-J. Meyer, *Zeitschrift fÃijr anorganische und allgemeine Chemie*, 2001, **627**, 2002–2004.

[36] H. D. Zhou, E. S. Choi, G. Li, L. Balicas, C. R. Wiebe, Y. Qiu, J. R. D. Copley and J. S. Gardner, *Physical Review Letters*, 2011, **106**, 147204.

[37] A. V. Sologubenko, E. Felder, K. Gianno, H. R. Ott, A. Vietkine and A. Revcolevschi, *Physical Review B*, 2000, **62**, R6108–R6111.

[38] H. F. Pen, J. van den Brink, D. I. Khomskii and G. A. Sawatzky, *Physical Review Letters*, 1997, **78**, 1323–1326.

[39] M. Dhariwal, T. Maitra, I. Singh, S. Koley and A. Taraphder, *Solid State Communications*, 2012, **152**, 1912–1916.

[40] W. Tian, M. F. Chisholm, P. G. Khalifah, R. Jin, B. C. Sales, S. E. Nagler and D. Mandrus, *Materials Research Bulletin*, 2004, **39**, 1319–1328.

[41] R. Pocha, D. Johrendt, B. Ni and M. M. Abd-Elmeguid, *Journal of the American Chemical Society*, 2005, **127**, 8732–8740.

[42] T. Waki, Y. Kajinami, Y. Tabata, H. Nakamura, M. Yoshida, M. Takigawa and I. Watanabe, *Physical Review B*, 2010, **81**, 020401.

[43] S. Nakatsuji, K. Kuga, K. Kimura, R. Satake, N. Katayama, E. Nishibori, H. Sawa, R. Ishii, M. Hagiwara, F. Bridges, T. U. Ito, W. Higemoto, Y. Karaki, M. Halim, A. A. Nugroho, J. A. Rodriguez-Rivera, M. A. Green and C. Broholm, *Science*, 2012, **336**, 559–563.

[44] Y. Shirata, H. Tanaka, A. Matsuo and K. Kindo, *Physical Review Letters*, 2012, **108**, 057205.

[45] L. J. Sandilands, Y. Tian, K. W. Plumb, Y.-J. Kim and K. S. Burch, *Physical Review Letters*, 2015, **114**, 147201.

[46] J. A. Sears, M. Songvilay, K. W. Plumb, J. P. Clancy, Y. Qiu, Y. Zhao, D. Parshall and Y.-J. Kim, *Physical Review B*, 2015, **91**, 144420.

[47] A. Banerjee, C. A. Bridges, J.-Q. Yan, A. A. Aczel, L. Li, M. B. Stone, G. E. Granroth, M. D. Lumsden, Y. Yiu, J. Knolle, S. Bhattacharjee, D. L. Kovrizhin, R. Moessner, D. A. Tennant, D. G. Mandrus and S. E. Nagler, *Nature Materials*, 2016, **15**, 733–740.

[48] M. Abdel-Jawad, I. Terasaki, T. Sasaki, N. Yoneyama, N. Kobayashi, Y. Uesu and C. Hotta, *Physical Review B*, 2010, **82**, 125119.

[49] K. Miyagawa, A. Kawamoto and K. Kanoda, *Physical Review B*, 2000, **62**, R7679–R7682.

[50] M. Oshikawa, *Physical Review Letters*, 2000, **84**, 1535–1538.

[51] S. A. Parameswaran, A. M. Turner, D. P. Arovas and A. Vishwanath, *Nature Physics*, 2013, **9**, 299–303.

[52] K. S. Novoselov, A. K. Geim, S. V. Morozov, D. Jiang, Y. Zhang, S. V. Dubonos, I. V. Grigorieva and A. A. Firsov, *Science*, 2004, **306**, 666–669.

[53] K. S. Novoselov, V. I. FalâĂško, L. Colombo, P. R. Gellert, M. G. Schwab and K. Kim, *Nature*, 2012, **490**, 192–200.

[54] Q. H. Wang, K. Kalantar-Zadeh, A. Kis, J. N. Coleman and M. S. Strano, *Nature Nanotechnology*, 2012, **7**, 699–712.

[55] M. Chhowalla, H. S. Shin, G. Eda, L.-J. Li, K. P. Loh and H. Zhang, *Nature Chemistry*, 2013, **5**, 263–275.

[56] X. Qian, J. Liu, L. Fu and J. Li, *Science*, 2014, **346**, 1344–1347.

[57] M. N. Ali, J. Xiong, S. Flynn, J. Tao, Q. D. Gibson, L. M. Schoop, T. Liang, N. Haldolaarachchige, M. Hirschberger, N. P. Ong and R. J. Cava, *Nature*, 2014, **514**, 205–208.

[58] A. K. Geim and I. V. Grigorieva, *Nature*, 2013, **499**, 419–425.

[59] Y. Liu, N. O. Weiss, X. Duan, H.-C. Cheng, Y. Huang and X. Duan, *Nature Reviews Materials*, 2016, **1**, 16042.

[60] B. Radisavljevic, A. Radenovic, J. Brivio, V. Giacometti and A. Kis, *Nature Nanotechnology*, 2011, **6**, 147–150.

[61] C.-H. Lee, G.-H. Lee, A. M. van der Zande, W. Chen, Y. Li, M. Han, X. Cui, G. Arefe, C. Nuckolls, T. F. Heinz, J. Guo, J. Hone and P. Kim, *Nature Nanotechnology*, 2014, **9**, 676–681.

[62] F. Withers, O. Del Pozo-Zamudio, A. Mishchenko, A. P. Rooney, A. Gholinia, K. Watanabe, T. Taniguchi, S. J. Haigh, A. K. Geim, A. I. Tartakovskii and K. S. Novoselov, *Nature Materials*, 2015, **14**, 301–306.

[63] J. M. Rondinelli and N. A. Spaldin, *Advanced Materials*, 2011, **23**, 3363–3381.

[64] H. Watanabe, H. C. Po, A. Vishwanath and M. P. Zaletel, *arXiv:1505.04193*.

[65] S. A. J. Kimber, I. I. Mazin, J. Shen, H. O. Jeschke, S. V. Streltsov, D. N. Argyriou, R. Valenti and D. I. Khomskii, *Physical Review B*, 2014, **89**, 081408.

[66] L. N. Bulaevskii, A. I. Buzdin and D. I. Khomskii, *Solid State Communications*, 1978, **27**, 5–10.

[67] P. J. Baker, S. J. Blundell, F. L. Pratt, T. Lancaster, M. L. Brooks, W. Hayes, M. Isobe, Y. Ueda, M. Hoinkis, M. Sing, M. Klemm, S. Horn and R. Claessen, *Physical Review B*, 2007, **75**, 094404.

[68] M. C. Cross and D. S. Fisher, *Physical Review B*, 1979, **19**, 402–419.